Estimation of the sugar content of fruit by energy-resolved computed tomography using a material decomposition method

Ikuo Kanno* and Takahiro Kuroyama

Department of Nuclear Engineering, Graduate School of Engineering, Kyoto University, Katsura, Nishikyo, Kyoto 615-8530, Japan

*kanno@nucleng.kyoto-u.ac.jp

Estimation of the sugar content of fruit by energy-resolved computed tomography using a material decomposition method

We have been developing energy-resolved X-ray computed tomography (ER-CT) using a novel detector system called a transXend detector, which measures X-rays as electric current and gives the energy distribution of X-rays by unfolding analysis. This paper presents the results of the sugar content measurements of kiwifruit samples by ER-CT. Because the change of linear attenuation coefficients as a function of sugar content was small, we used a material decomposition method instead of the unfolding method to deduce the linear attenuation coefficient from the measured electric current. The obtained sugar contents showed good agreement with those measured by a refractometer.

Keywords: X-ray; computed tomography; energy distribution; material decomposition; non-destructive; experiment

1. Introduction

X-ray computed tomography (CT) is an effective modality to identify tumor tissue and anomalies inside the organs of human bodies. In CT inspections at hospitals, X-rays are measured as electric current without using the energy information of X-ray photons. This measurement method is called a current measurement. X-rays are attenuated according to the linear attenuation coefficient of a material. The linear attenuation coefficient is generally greater for X-rays of lower energy according to data from the National Institute of Standards and Technology (NIST) [1]. As X-rays pass through a material, the number of low-energy X-ray photons decreases more quickly than that of high-energy X-ray photons, causing the number of high-energy X-ray photons to dominate. As a result, the averaged energy of an X-ray energy spectrum increases after passing through a material. The measured linear attenuation coefficient of the material

changes as a function of the path length of the X-rays. This phenomenon is called the beam hardening effect [2].

To avoid the beam hardening effect, it is necessary to use the energy information of X-rays [3]. There are three ways to exploit the energy information of X-rays in CT: dual-energy CT (DE-CT), photon-counting CT (PC-CT) and energy-resolved CT (ER-CT).

DE-CT performs CT measurements twice with changing X-ray tube voltages [4]. The change of averaged X-ray energies is, however, not much. When using 80 kV and 140 kV tube voltages, typical averaged energies are 42.4 keV and 58.2 keV, respectively. DE-CT gives not enough energy information. Moreover, DE-CT results in large exposure dose due to two exposures. As an alternative of DE-CT, dual-layer detector is used to give linear attenuation coefficients for high and low energy X-rays [5]. Again, the difference of averaged energies measured by the upper and lower detector is not much.

In PC-CT, the energy of each incident X-ray photon is measured and sorted into 6 to 8 energy bins. The number of X-rays coming into a CT detector, however, is too high to perform the energy measurement of each X-ray photon. With this difficulty, the photon counting CT is under study with suppressed counting rate [6]. The systems of PC-CT are in the pre-clinical investigation stage [7]. To compete with DE-CT, further improvement is necessary [8].

We have been studying energy-resolved X-ray computed tomography (ER-CT) using a novel detector system called a “transXend” detector [9]. The transXend detector consists of multiple segmented detectors aligned in the direction of X-ray incidence as shown in Figure 1 of Ref. [9]. We call this a stacked-type transXend detector. Because each segmented detector measures X-rays as electric current, the

transXend detector has no problems associated with the huge number of incident X-rays. Using the previously obtained response functions for each segmented detector as a function of X-ray energy, the energy distribution of incident X-rays can be estimated by an unfolding method for the X-ray energy with 0.5 keV or 1 keV interval. We measured the linear attenuation coefficients of nine kinds of resins and estimated their effective atomic numbers (Z_{eff}), which ranged from 5 to 14 with the errors of Z_{eff} were within 3% [10].

Apart from the stacked-type transXend detector for the measurement with pencil beam X-rays, we developed a two-dimensional transXend detector with a flat panel detector (FPD) and two kinds of ribbon metal absorbers in lattice structure in front of the FPD [11]. For CT measurements with the stacked-type transXend detector, a phantom was scanned by pencil beam X-rays with the movements of translation and rotation. This measurement takes long time. With the two-dimensional transXend detector, the phantom is scanned by fan beam or cone beam X-rays with the rotation movement. The two-dimensional transXend detector has an advantage of shorter measurement time, which advantage is the same one for the third generation CT to the first generation CT.

We measured Z_{eff}s of eleven RMI rods (Gammex, Middleton, WI, US) which were developed by Constantinou, et al. [12] with ER-CT method. Z_{eff}s of rod materials were measured within $\pm$1.8% error after the normalization with the one of breast [13]. Similar measurements were performed by some groups with using the RMI rods by clinical CT scanners with DE-CT method. Bazalova et al. performed DE-CT with 100 kV and 140 kV tube voltages and reported Z_{eff} with averaged error 2.8%, with the largest error 12.0% [14]. Goodsitt et al. used rapid kVp switching DE-CT method and

gave errors of -6% to +6% for phantoms with $Z_{eff} > 6.3$, and the errors of 15% for phantoms with $Z_{eff} < 6.3$, respectively [15].

In this paper, we describe a method to use ER-CT to estimate the sugar content of fruit as a precise measurement of Z_{eff}. The Z_{eff}s of fructose and water are 6.95 and 7.42, respectively. Similar to the Z_{eff} estimation of resins, sugar content is determined by measuring the linear attenuation coefficient of a sample. However, the change of the linear attenuation coefficient as a function of sugar content is small. To distinguish small differences of linear attenuation coefficients, we employ a material decomposition method to analyze the ER-CT data instead of unfolding the X-ray energy distribution, which we used previously.

Generally, sugar content is measured in the unit of degrees Brix (°Bx); the sugar content of a 100-g solution containing 1 g of sucrose at 20 °C is defined 1 °Bx. Sucrose consists of glucose and fructose, which are isomers of each other.

Sugar content measurement methods include destructive and non-destructive approaches. A sugar content meter that measures the refractive index of liquids, i.e., the juice of a fruit, is a destructive method and has an accuracy of 0.1%–0.2% [16]. Infrared (IR) spectroscopy is a non-destructive method to estimate the sugar content of fruit that involves with measuring the absorption spectrum of IR light and estimating sugar content using the previously obtained calibration line of IR light absorption. However, IR spectroscopy has some disadvantages, including measurement error caused by the variation of fruit samples from those used to make the calibration line and restricted measurement region that is limited to the fruit surface where IR light can reach. A typical commercial IR Brix meter has an accuracy of 1.0%–1.5% [16]. ER-CT is also a non-destructive method and can give sugar content distribution including

the center part of a fruit where IR light can't reach. Our goal is to estimate the sugar content of fruit samples with accuracy of 1.0%.

In this report, we first describe a method to estimate the sugar content of fructose solutions in an acrylic (PMMA) container using standard phantoms. After establishing this method, it is used to estimate the sugar content of kiwifruit samples.

2. Materials and Methods

2.1 Experimental setup for ER-CT

The experimental setup for ER-CT is shown in Figure 1. The X-ray tube (TRIX-150S, Toreck Co., Ltd., Yokohama, Japan) had a W target with a colliding angle of 22°. This X-ray tube had a 1 mm thick Be filter. An additional Al filter with a thickness of 2 mm was included in the system to decrease the number of low-energy X-rays. A rotating wheel consisting of a PMMA disk with a thickness of 1 mm was placed at the X-ray tube exit to change the X-ray energy spectra. The rotating wheel was divided into four regions—one uncovered region and three covered with Cu filters with thicknesses of 0.1, 0.2, and 0.3 mm—which provided four different X-ray energy spectra.

X-rays were measured by a flat panel detector (FPD; Remote RadEye2, Teledyne Rad-icon Imaging, Santa Clara CA, USA). The FPD contained a 1024×1024 array of 48×48 μm silicon photodiode pixels. The sensitive area of the FPD was 48.2 × 48.2 mm. X-rays were absorbed by a Gd_2O_2S (GOS) scintillator plate with an effective thickness of 50 μm. Scintillation photons were detected by the photodiode pixels.

The FPD and a region on the rotating wheel corresponded to a segmented detector of the stacked-type transXend detector; thus, the two-dimensional transXend detector in this experimental setup had four segmented detectors. Each segmented

detector is hereafter denoted as a channel: Cu filters with thicknesses of 0, 0.1, 0.2, and 0.3 mm correspond to channel 1, 2, 3, and 4, respectively. X-ray spectra for channel 1 and 4 calculated using the formula of Birch et al. [17] are shown in Figure 2.

To suppress scattered X-rays, a 1-mm-thick W plate with a horizontal opening with a width of 4 mm was placed between the X-ray tube and a phantom. The phantom was placed on a precision rotating stage (SGSP-60YAW, Sigma Koki, Tokyo, Japan) for CT measurements from 36 angles. The operating conditions of the X-ray tube were 100 kV, 2.4 mA, and 0.5 s for each CT measurement angle.

2.2 Standard phantoms for sugar content measurements

As preparation for the sugar content estimation of fruit samples by ER-CT, fructose solutions were used as known liquid. Fructose solutions with various sugar contents were added to a hole with a 15-mm diameter in a PMMA cylinder with a diameter of 30 mm to form standard phantoms.

The chemical formula of fructose is $C_6H_{12}O_6$ and its effective atomic number is 6.95 according to an empirical formula reported by Mayneord [18]. We made fructose solutions with mass percent concentrations of 5%, 10%, 15%, and 30%. The sugar contents of these solutions were measured by a sugar refractometer (APAL-J, Atago, Tokyo, Japan). The measured sugar contents for the 5%, 10%, 15%, and 30% solutions were 4.9, 9.8, 15.0, and 29.7 $\pm$ 0.2 °Bx, respectively.

2.3 Analysis

2.3.1 Response functions

To estimate X-ray energy spectra after passing through a phantom with various paths, response functions for each channel are necessary. Response functions were estimated using the measured electric currents induced by X-rays that passed through reference

PMMA slabs with thicknesses of 10, 20, 30, and 40 mm which are denoted as reference material No. 1, 2, 3, and 4, respectively.

The electric current measured after passing through the *j*-th reference material in the *i*-th channel is written as

$$I_{i,j} = a \int Y(E) R_i(E) \exp\{-\mu_P(E) t_j\} dE + b. \quad (1)$$

Here, $Y(E)$ is the number of X-ray photons with energy E emitted by the X-ray tube, $R_i(E)$ is the response function of *i*-th channel, $\mu_P(E)$ is the linear attenuation coefficient of PMMA, and t_j is the thickness of PMMA as the *j*-th reference material. Also, a and b are the correction factors for gain and offset, respectively. The X-ray spectrum $Y(E)$ is calculated as,

$$Y(E) = Y_0(E) \exp\{-\mu_{Al}(E) t_{Al} - \mu_W(E) t_W\}. \quad (2)$$

Here, $Y_0(E)$ is the X-ray energy spectrum calculated using the formula developed by Birch et al., $\mu_{Al}(E)$ and $\mu_W(E)$ are the linear attenuation coefficients of Al and W, respectively, and t_{Al} and t_W are the thicknesses of Al and W, respectively, used to correct $Y_0(E)$ to reproduce measured electric current. The W thickness correction is for taking into account the Heel effect, which is influenced by the X-ray path length inside the W target. [19] The response function $R_i(E)$ can be written as,

$$R_i(E) = R_0(E) \exp\{-\mu_{Cu}(E) t_i c_i\}, \quad (3)$$

where $R_0(E)$ is the energy deposited in the GOS scintillator by an X-ray photon with energy E calculated by the GEANT4 Monte Carlo code [20] and $\mu_{Cu}(E)$, t_i, and c_i are the linear attenuation coefficient of Cu, the thickness of the Cu filter, and the correction factor for the thickness of the *i*-th channel Cu filter (*i*=1, 4), respectively.

We determined correction factors, a, b, t_{Al}, t_{W}, c_1, c_2, c_3 and c_4 by minimizing the following relationship,

$$S = \sum_{i,j} \left(I_{i,j}^{meas.} - I_{i,j} \right)^2. \quad (4)$$

Here, $I_{i,j}^{meas.}$ is the measured electric current for X-rays passing through the *j*-th reference material in the *i*-th channel, which was averaged over horizontal pixels of the FPD from 1 to 1024 and also averaged vertically from the 486th to the 500th lines of pixels in the FPD to avoid the possible fluctuation of pixel values. Schematic drawing of this process is shown in Figure 3. Obtained response functions are shown in Figure 4.

2.3.2 Material decomposition method

In this study, we used a material decomposition method to estimate the X-ray energy distribution after passing through a phantom. As shown in Figure 1, the measured electric current induced by X-rays in the *k*-th horizontal pixel of the FPD at the *l*-th rotating angle of the phantom in the *i*-th channel is written as,

$$I_{i,k,l} = a \int Y(E) R_i(E) \exp\{-\mu_{k,l}(E) d_{k,l}\} dE + b. \quad (5)$$

The thicknesses of PMMA and the fructose solution change according to the measurement position (*k*,*l*). We measured four electric currents for each measurement position (*k*,*l*). However, we have 161 unknown $\mu_{k,l}(E)d_{k,l}$, because we estimated the X-ray energy spectrum every 0.5 keV from 20 to 100 keV. It is therefore very difficult to determine $\mu_{k,l}(E)d_{k,l}$ from only four measurement values at each measurement position (*k*,*l*) by unfolding analysis.

To overcome this difficulty, we reproduced $\mu_{k,l}(E)d_{k,l}$ using the linear attenuation coefficients of hydrogen $\mu_H(E)$ and oxygen $\mu_O(E)$: Z_{eff} of fructose solutions ranges from 6.95 (fructose) to 7.42 (water) and that of PMMA is 6.47. The atomic numbers of hydrogen and oxygen are 1 and 8, respectively, and Z_{eff} of the fructose solutions and PMMA are between these values. The linear attenuation coefficient of a material with Z_{eff} between 1 and 8 can be reproduced by the linear combination of

$\mu_H(E)$ and $\mu_O(E)$. For example, the linear attenuation coefficient of carbon is reproduced as,

$$\mu_C(E) = 6.4 \times 10^3 \mu_H(E) + 4.8 \times 10^2 \mu_O(E), \quad (6)$$

as shown in Figure 5.

Equation (5) can be rewritten using $\mu_H(E)$ and $\mu_O(E)$ as,

$$I_{i,k,l} = a \int Y(E) R_i(E) \exp\{-\mu_H(E) d_{k,l}^H - \mu_O(E) d_{k,l}^O\} dE + b. \quad (7)$$

Here, $d_{k,l}^H$ and $d_{k,l}^O$ are the thicknesses of hydrogen and oxygen, respectively, to reproduce the X-ray attenuation at measurement position (*k*,*l*). To estimate unknown values $d_{k,l}^H$ and $d_{k,l}^O$, we prepared look-up tables (LUTs) for the thicknesses of hydrogen and oxygen, d^H and d^O, respectively, for each channel. We estimated $d_{k,l}^H$ and $d_{k,l}^O$ by finding d^H and d^O that minimized the following equation,

$$S_{k,l} = \sum_{i=1}^{4} \{I_{k,l}^{meas.,i} - I^i(d^H, d^O)\}^2, \quad (8)$$

with changing d^H and d^O from zero value to their maximums, $d^{H,max}$ and $d^{O,max}$. The electric current $I_{k,l}^{meas.,i}$ was obtained by averaging vertically from the 486th to the 500th lines of the pixels in the FPD. $I^i(d^H, d^O)$ is the electric current value in the LUT prepared for the *i*-th channel as functions of d^H and d^O. The schematic drawing of finding d^H and d^O is shown in Figure 6.

2.3.3 Water phantom correction

Sugar content was estimated by comparing measured and theoretical linear attenuation coefficients. Measured linear attenuation coefficients were obtained from the ER-CT images as CT values as a function of X-ray energy. To have correct CT values, the transmission measurement of X-rays through water should be the same as that

227 calculated using the Lambert–Beer law [21]. Figure 7 shows the theoretical and
228 experimental results of X-ray transmission through a water phantom (i.e., zero sugar
229 content). Although the results in Figure 7 look fairly similar, they differ slightly because
230 of X-ray scattering and other effects. The ratio of theoretical to experimental values is
231 presented in Figure 8. This ratio was applied to all measured results as the water
232 phantom correction factor.
233

234 ***2.4 Sugar contents of standard phantoms***

235 A reconstructed CT image using the number of X-ray photons with an energy of 70 keV
236 for a 10% fructose solution is shown in Figure 9. The CT value of this image shows the
237 linear attenuation coefficient for X-rays with an energy of 70 keV. By assigning a
238 50×50 pixel region in the fructose solution as the region of interest (ROI), the linear
239 attenuation coefficient as a function of X-ray energy was obtained as the averaged CT
240 value in the ROI. The linear attenuation coefficients for 5%, 15%, and 30% fructose
241 solutions as a function of X-ray energy are displayed in Figure 10. Error bars given by
242 the standard deviations of the CT values in ROIs are only shown for the linear
243 attenuation coefficient of the 30% fructose solution because the error bars for the linear
244 attenuation coefficients were similar for all solutions with different sugar contents.

245 To determine the sugar content of each solution, we prepared reference curves of
246 the linear attenuation coefficients as a function of X-ray energy, $\mu_{ref.}(f_i, E_j)$, for
247 fructose solutions with the concentration of f_i with 0.1% intervals from 0 to 30% by
248 calculations using data from NIST [1]. The sugar content of fructose solutions was
249 estimated by finding $\mu_{ref.}(f_i, E_j)$ which gives the minimum value of $S_s(f_i)$ in the
250 following equation,

$$S_s(f_i) = \sum_{j=1}^{101}\{\mu_{meas.}(E_j) - \mu_{ref.}(f_i, E_j)\}^2. \quad (9)$$

Here, $\mu_{meas.}(E_j)$ is the measured linear attenuation coefficient at energy E_j. We used linear attenuation coefficients for X-ray photon energies from 40 to 90 keV for the sugar content estimation because of the small numbers of X-ray photons with energies below 40 keV and above 90 keV. Estimated sugar contents are shown in Figure 11. The calibration line obtained using least squares fitting is drawn as a solid line. The dashed lines show the limitation of ±1% from the calibration line.

Flow chart of sugar content estimation method is shown in Figure 12.

2.5 Sugar content measurements of kiwifruit

We applied the sugar content estimation method described above to two kiwifruit samples. Because the dimensions of the sensitive area of our FPD was 48.2×48.2 mm and the diameters of commercially available kiwifruits are greater than 50 mm, we cut kiwifruit samples out with diameters of less than 24 mm and put them in PMMA casings with inner and outer diameters of 24 and 30 mm, respectively: in the CT measurement, the attenuation of X-rays was measured as the ratio of the electric current induced by X-rays after transmitting through a sample to that of X-rays passing through air. Photographs of the prepared kiwifruit samples are depicted in Figure 13. To estimate the sugar contents of both the green and white parts of the kiwifruit samples, we cut samples off the axis of kiwifruits.

The ER-CT images reconstructed from the number of X-rays with an energy of 70 keV are shown in Figure 14. We defined two ROIs for each CT image, which corresponded to the green (ROI_G) and white (ROI_W) parts of the kiwifruit samples. Each ROI had 50×50 pixels. Obtained linear attenuation coefficients for the kiwifruit

samples are shown in Figure 15. Error bars are shown only for the linear attenuation coefficients of green parts because those for the white parts had nearly the same lengths.

Using Equation (9), the sugar contents of the kiwifruit samples were estimated. The estimated sugar contents of the green part of the kiwifruit samples are presented in Figure 11, in which the *x*-values show those measured by the refractometer for juice squeezed from the green part of each sample.

3. Results and Discussion

The transmission measured for the water phantom looked to agree well with the theoretical one in Figure 7; however, the slight difference between them is shown in Figure 8. The cause of this difference is not obvious, but we think that scattered X-rays may be the main reason. Large deviations can be seen for the pixel number 115 and 903. This is because the borders of these pixels did not match with that between PMMA and water. We consider that this difference is a geometric effect. Therefore, a geometrical correction was carried out by multiplying all the measured transmission data by this factor.

Ring artifacts are seen in Figure 9. We think the artifacts were brought by the small number of X-ray photons and also the small number of projection angles. Similar artifacts are seen in Figure 14.

Figure 10 displays the error bars at every 10 keV for the linear attenuation coefficient of 30% fructose solution. The error bar at 40 keV was the smallest. We think the smallest error bar was observed at 40 keV because of the large number of X-ray photons of this energy in channel 1 (i.e., without a Cu filter), as shown in Figure 2. The error bars are larger than those of Figure 5 of Ref. [10]. In Ref. [10], the X-rays were collimated by two W collimators with a diameter of 1 mm. In this case, the X-ray

299 path was well defined so there was almost no effect from scattered X-rays. In the
300 estimation of fruit sugar content or the ER-CT imaging of a human body, however, we
301 have to use a two-dimensional transXend detector, so the influence of X-ray scattering
302 cannot be avoided. The development of an algorithm that omits scattered X-rays will be
303 the focus of our future study.

304 It may be possible to estimate the error of sugar content values by fitting linear
305 attenuation coefficients taking the upper and lower values of error bars. However, this
306 estimation does not have much meaning. Because the center value of linear attenuation
307 coefficients changes according to the sugar content of the samples, we believe that our
308 ER-CT measurements were performed properly and the error was systematic: small
309 number of X-ray photons.

310 The sugar contents of the green parts of kiwifruit samples showed good
311 agreement with those measured by the refractometer within the error of 1% from the
312 calibration line, which was the purpose of this study. We could not extract juice from
313 the white parts of the kiwifruit samples but had white suspension, so we could not
314 measure their sugar content with the refractometer. The sugar content estimated by ER-
315 CT was 1.1 °Bx for the white part of kiwifruit sample (a). The linear attenuation
316 coefficient of the white part of kiwifruit sample (b) was smaller than that of water so we
317 could not estimate its sugar content. The estimated Z_{eff} of the white part of kiwifruit
318 sample (b) was 7.72, which was greater than that of water (7.42).

319 Using ER-CT, we can obtain the distribution of sugar content in a fruit sample.
320 The green and white parts of a kiwifruit showed different sugar contents. In IR
321 spectroscopy, sugar content can be measured only for regions close to the fruit surface.
322 Therefore, the sugar content measurement by ER-CT has an advantage over that
323 determined by IR spectroscopy regarding this point. The developed sugar content

estimation method using ER-CT can be used for other non-destructive food inspections such as fat content measurement. To extend the application of the two-dimensional transXend detector, a method to suppress the effect of X-ray scattering should be developed in the future.

Acknowledgment

We thank Dr. Y. Yamashita, Osaka Prefecture University College of Technology, for fruitful discussion. We acknowledge The Kansai Atomic Conference for financial support.

References

[1] Hubbell JH, Seltzer SM. Tables of X-ray mass attenuation coefficients and mass energy-absorption coefficients from 1 keV to 20 MeV for elements Z = 1–92 and 48 additional substances of dosimetric interest. The Physical Measurement Laboratory, The National Institute of Standard and Technology; 2010. Available from: http://www.nist.gov/pml/data/xraycoef/index.cfm

[2] Brooks RA, Di Chiro G. Beam hardening in X ray reconstructive tomography. Phys Med Biol. 1976;21:390–398.

[3]Poumorteza A, Syons R, Sandfort V., et al. Abdominal imaging with contrast-enhanced photon-counting CT:First human experience. Radiol. 2016;279:239-245.

[4] Bazalova M, Carrier J-F, Beaulier L, et al. Tissue segmentation in Monte Carlo treatment planning: a simulation study using dual-energy CT images. Radiother Oncol. 2008;86:93-98.

[5] van Elmpt W, Landry G, Das M, et al. Dual energy CT in radiotherapy: current applications and future outlook. Radiother Oncol. 2016;119:137-144.

[6] Le HQ, Ducote JL, Molloi S. Radiation dose reduction using a CdZnTe-based computed tomography system: comparison to flat-panel detectors. Med Phys. 2010; 37: 1225-1236.

[7] de Vries A, Roessl E, Kneepkens E, et al. Quantitative spectral K-edge imaging in preclinical photoncounting X-ray computed tomography. Invest Radiol. 2015;50:297-304.

[8] Atak H, Shikhaliev PM. Dual energy CT with photon counting and dual source systems: comparative evaluation. Phys Med Biol. 2015;60:8949-8975.

[9] Kanno I, Imamura R, Mikami K, et al. A current mode detector for unfolding X-ray energy distribution. J Nucl Sci Technol. 2008;45:1165-1170.

[10] Hamaguchi T, Kanno I. Effective atomic number estimation by energy-resolved X-ray computed tomography with a current-mode detector system. Jpn J Appl Phys. 2019; 58: 071001-6.

[11] Kanno I, Yamashita Y, Kanai E, Ogawa T, Shinsho K. Two-dimensional "transXend" detector for third-generation energy-resolved computed tomography. J Nucl Sci Tehcnol. 2016;53:258-262.

[12] Constantinou C, Attix FH, Paliwal B. A solid water phantom material for radiotherapy x-ray and gamma ray beam calibrations. Med Phys. 1982;9:436-441.

[13] Iramina H, Nakamura M, Mizowaki T, Kanno I. Effective atomic number measurement with energy-resolved computed tomography using two-dimensional "transXend" detector. Int J Med Phys Clin Eng Radiat Oncol. 2018;7:61-73.

[14] Bazalova M, Carrier JF, Beaulieu L, Varhaegen F. Dual-energy CT-based metarial extraction for tissue segmentation in Monte Carlo dose calculations. Phys Med & Biol. 2008;53:2439-2456.

[15] Goodsitt MM, Christodoulou EG, Larson SC. Accuracies of the synthesized monochromatic CT numbers and effective atomic numbers obtained with a rapid kVp switching dual energy CT scanner. Med Phys. 2011;38:2222-2232.

[16] https://www.atago.net/en/pdf/tanpin-catalog/pal-hikari5_10_12_en.pdf.

[17] Birch R, Marshall M. Computation of bremsstrahlung X-ray spectra and comparison with spectra measured with a Ge(Li) detector. Phys Med Biol. 1979;24:505-517.

[18] Mayneord W V. The significance of the Röntgen. Acta Int. Union against Cancer 1937;2: 271-282.

[19] Buzug T M. Computed Tomography, Heidelberg:Springer; 2010.

[20] Agostinelli S, Allison J, Amako K, et al. GEANT4 –a simulation toolkit. Nucl Instrum Methods Phys Res. 2003;A506:250-303.

[21] Hsieh J. Computed tomography. 2nd ed. Washington:SPIE Press; 2009.

Figure captions

Figure 1. Experimental setup for sugar content measurements using a two-dimensional transXend detector with four channels.

Figure 2. Calculated X-ray energy spectra for channel 1 and 4.

Figure 3. Schematic drawing of determining correction factors. Correction factors, $a, b, t_{Al}, t_W, c_1, c_2, c_3, c_4$ are determined as the ones which result in the minimum *S* while changing the values of correction factors.

Figure 4. Response functions of the transXend detector for each channel. The valleys at 50 keV correspond to the K-edge of Gd.

Figure 5. The linear attenuation coefficient of carbon (solid line) reproduced by a linear combination of those of hydrogen (dashed line) and oxygen (dotted line) given by NIST. Solid circles are the theoretical linear attenuation coefficient of carbon taken from NIST data.

Figure 6. Schematic drawing of material decomposition, i.e., finding the thicknesses of hydrogen and oxygen to reproduce the X-ray attenuation by a subject. (m, n) in a small square mean the estimated electric current with taking into account the X-ray attenuation with the thicknesses of hydrogen, $d^{H,m}$ and oxygen, $d^{O,n}$ in i-th channel. $d^{H,max}$ and $d^{O,max}$ are the maximum values of hydrogen and oxygen thicknesses prepared for the look up table.

423

424 Figure 7. Measured and theoretically obtained electric current induced by X-rays after
425 transmitting a water phantom.

426

427 Figure 8. Correction factor for the water phantom obtained as the ratio of theoretical
428 value to measured value in Figure 7.

429

430 Figure 9. ER-CT image reconstructed for the number of X-rays with an energy of 70
431 keV for 10% fructose solution in an acrylic cylinder.

432

433 Figure 10. Measured linear attenuation coefficients for 5%, 15%, and 30% fructose
434 solutions as the averaged values of 50×50 pixel ROI in ER-CT images obtained at
435 intervals of 0.5 keV from 20 to 90 keV. Error bars are shown only for 30% fructose
436 solution every 10 keV.

437

438 Figure 11. Estimated sugar contents of 5%, 10%, 15%, and 30% fructose solutions
439 (open circles) and the green parts of two kiwifruit samples (solid circles). The solid line
440 is the calibration line given by the least squares fitting. Dashed lines show the ±1%
441 ranges from the calibration line.

442

443 Figure 12. Flow chart of sugar content estimation. “LUT” means look up table.

444

445 Figure 13. Photographs of kiwifruit samples in acrylic casings.

446

Figure 14. ER-CT images of kiwifruit samples reconstructed from the number of X-rays with an energy of 70 keV. ROIs for green and white parts are shown.

Figure 15. Obtained linear attenuation coefficients for green (solid lines) and white (dashed lines) parts of kiwifruit samples. Error bars are only shown for the linear attenuation coefficients for the green part every 10 keV. The error bars for the white part had similar values.

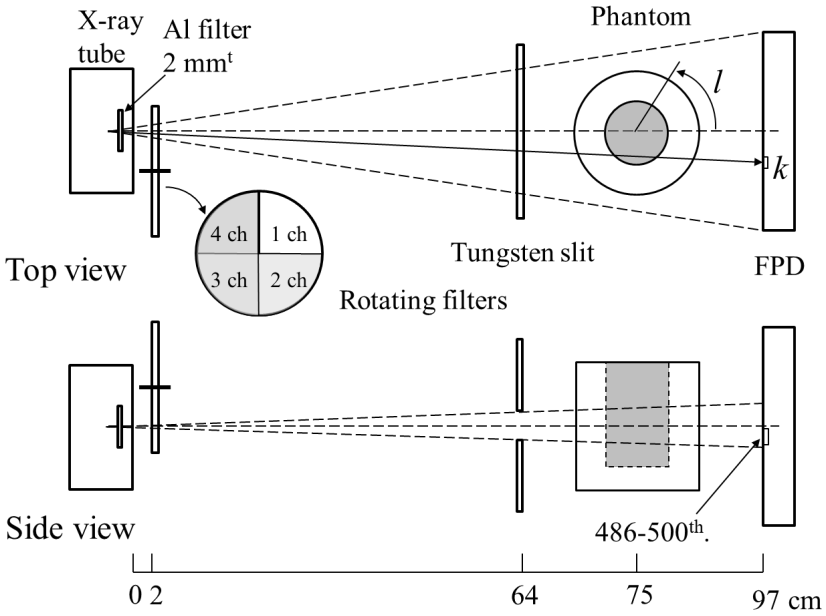
X-ray tube
Al filter 2 mm^{t}
Phantom
l
k
4 ch
1 ch
3 ch
2 ch
Top view
Tungsten slit
FPD
Rotating filters
Side view
486-500th.
0 2
64
75
97 cm

Figure 1

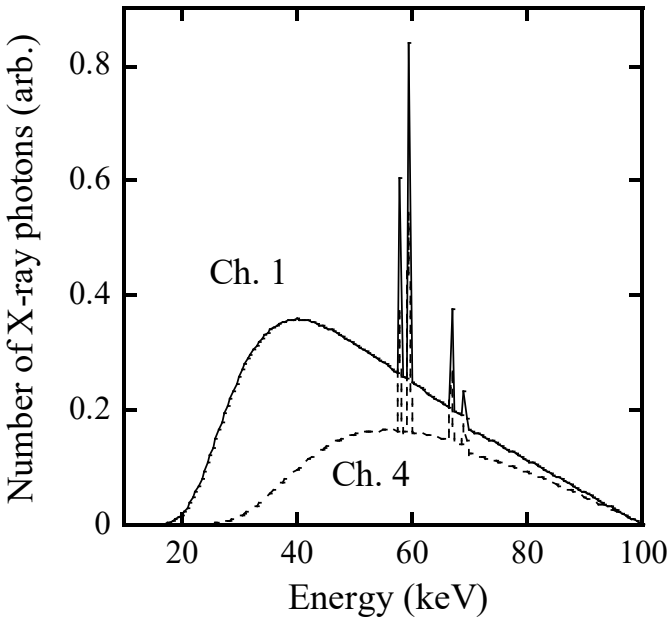
Number of X-ray photons (arb.)
0.8
0.6
0.4
0.2
0
Ch. 1
Ch. 4
20
40
60
80
100
Energy (keV)

Figure 2

4	$I_{1,4}$	$I_{2,4}$	$I_{3,4}$	$I_{4,4}$
3	$I_{1,3}$	$I_{2,3}$	$I_{3,3}$	$I_{4,3}$
2	$I_{1,2}$	$I_{2,2}$	$I_{3,2}$	$I_{4,2}$
1	$I_{1,1}$	$I_{2,1}$	$I_{3,1}$	$I_{4,1}$
j / i	1	2	3	4

$$S = \sum_{i,j} \left(I_{i,j}^{meas.} - I_{i,j} \right)^2$$

Minimizing S

$$a,\ b,\ t_{\mathrm{Al}},\ t_{\mathrm{W}},\ c_1,\ c_2,\ c_3,\ c_4$$

Figure 3

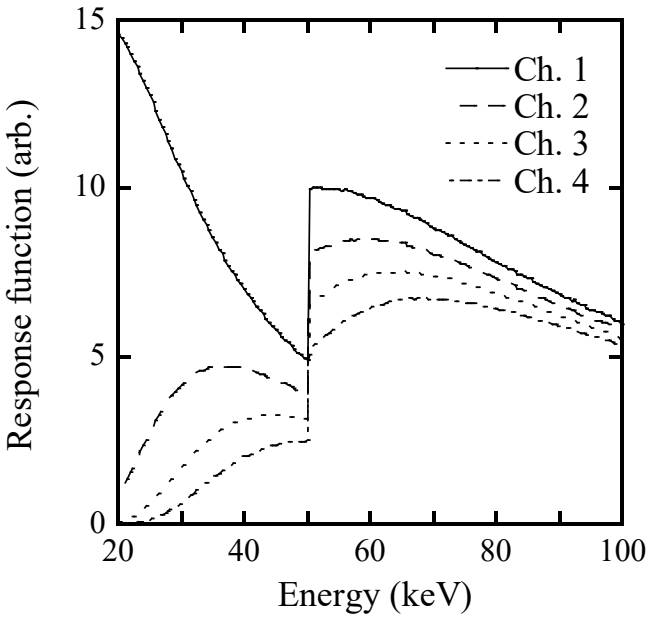
Response function (arb.)
Energy (keV)
Ch. 1
Ch. 2
Ch. 3
Ch. 4
0
5
10
15
20
40
60
80
100

Figure 4

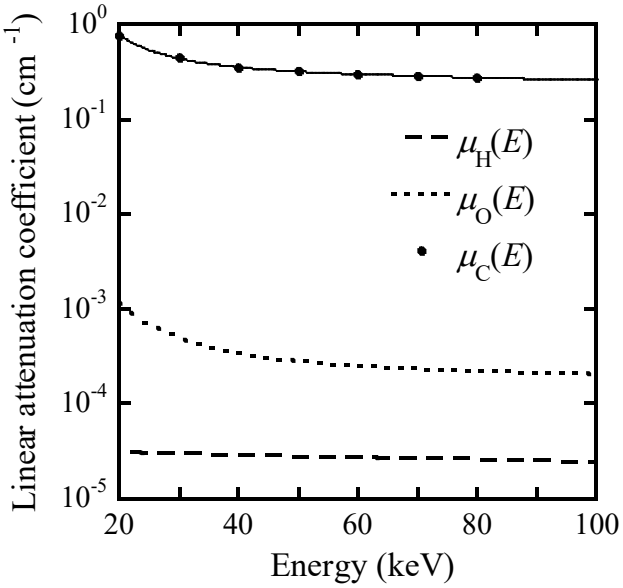
Linear attenuation coefficient (cm -1)
10^0
10^-1
10^-2
10^-3
10^-4
10^-5
20
40
60
80
100
Energy (keV)
μH(E)
μO(E)
μC(E)

Figure 5

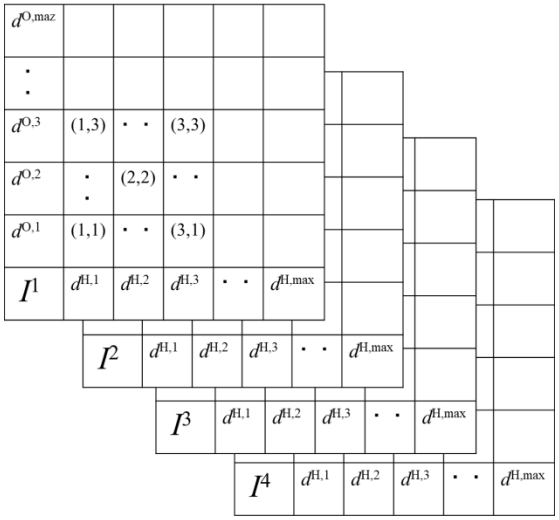

$$S_{k,l} = \sum_{i=1}^{4} \left\{ I_{k,l}^{meas,i} - I^i(d^H, d^O) \right\}^2$$

Search minimum $S_{k,l}$ in

$$0 \le d^H \le d^{H,max}, \qquad 0 \le d^O \le d^{O,max}$$

Figure 6

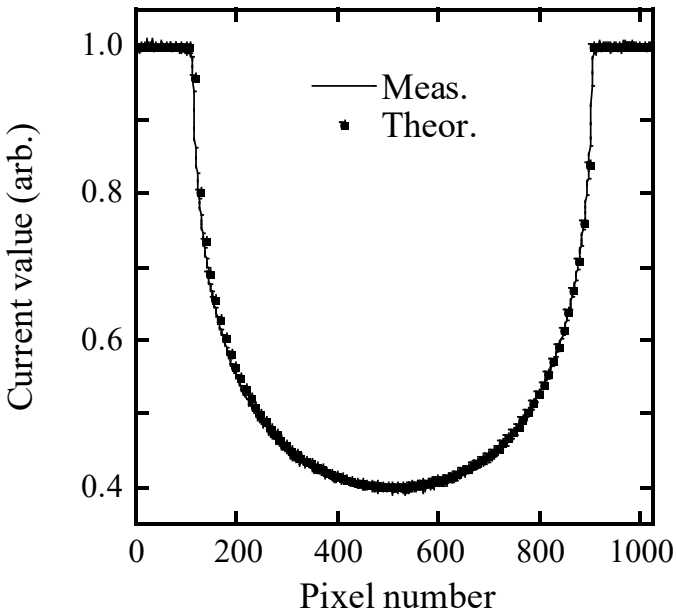
1.0
0.8
0.6
0.4
Current value (arb.)
Meas.
Theor.
0
200
400
600
800
1000
Pixel number

Figure 7

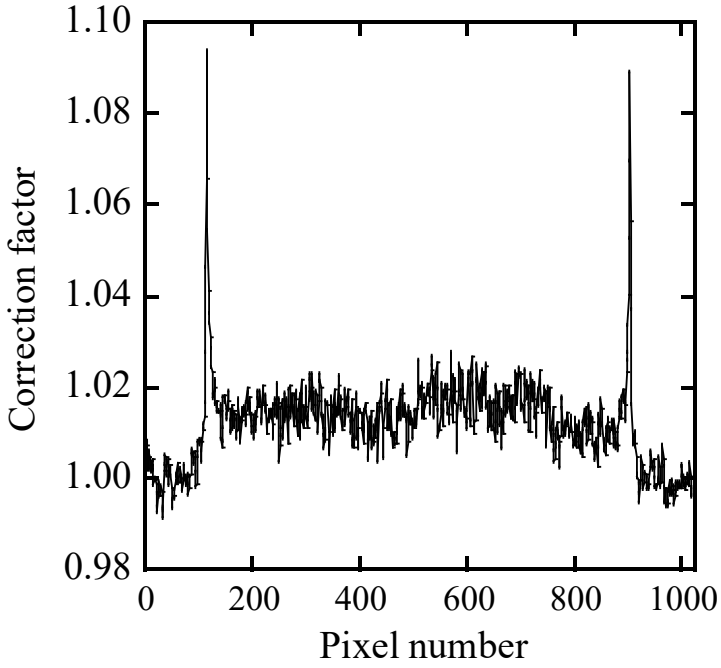
1.10
1.08
1.06
1.04
1.02
1.00
0.98
Correction factor
0
200
400
600
800
1000
Pixel number

Figure 8

598

599

600

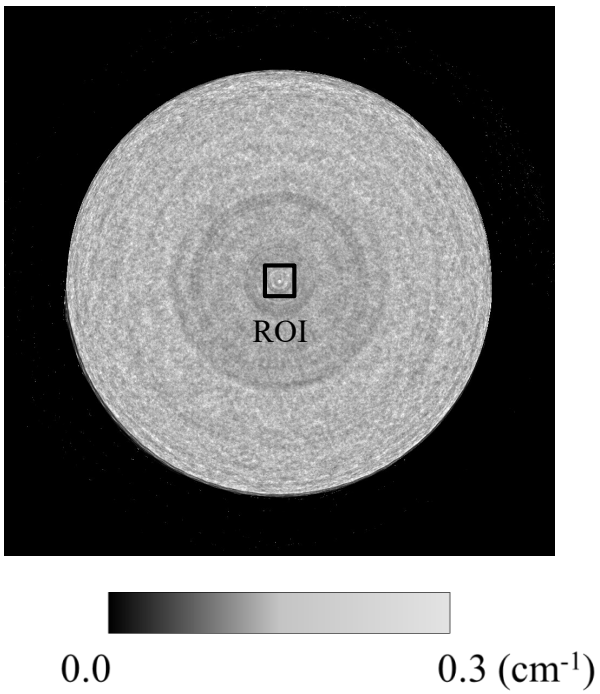

601

602

603

604

605

606

607 Figure 9

608

609

610

611

612

613

614

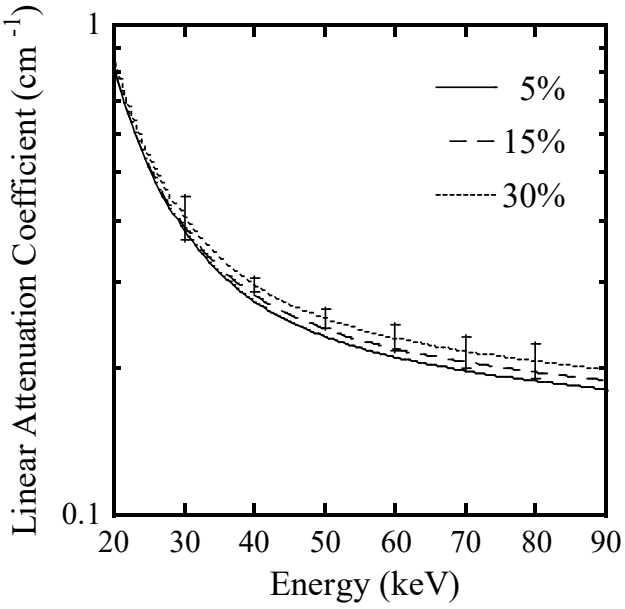
Linear Attenuation Coefficient (cm -1)
1
0.1
20
30
40
50
60
70
80
90
Energy (keV)
5%
15%
30%

Figure 10

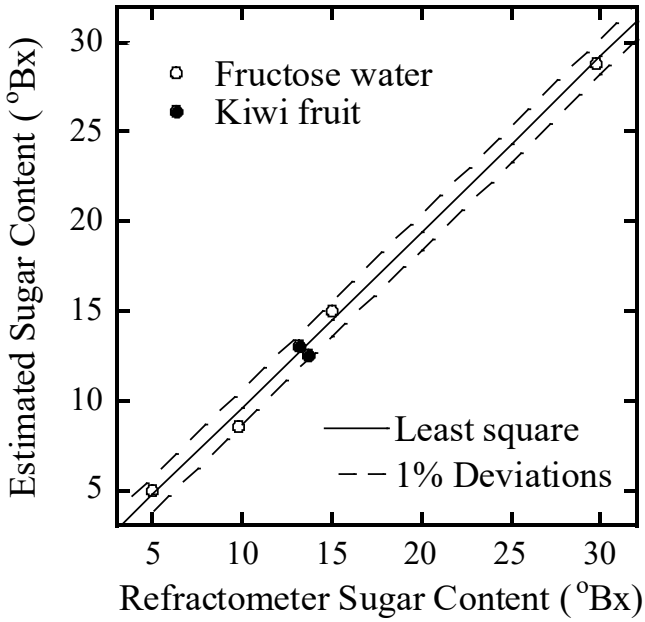
Estimated Sugar Content (°Bx)
Refractometer Sugar Content (°Bx)
Fructose water
Kiwi fruit
Least square
1% Deviations
5
10
15
20
25
30

Figure 11

649

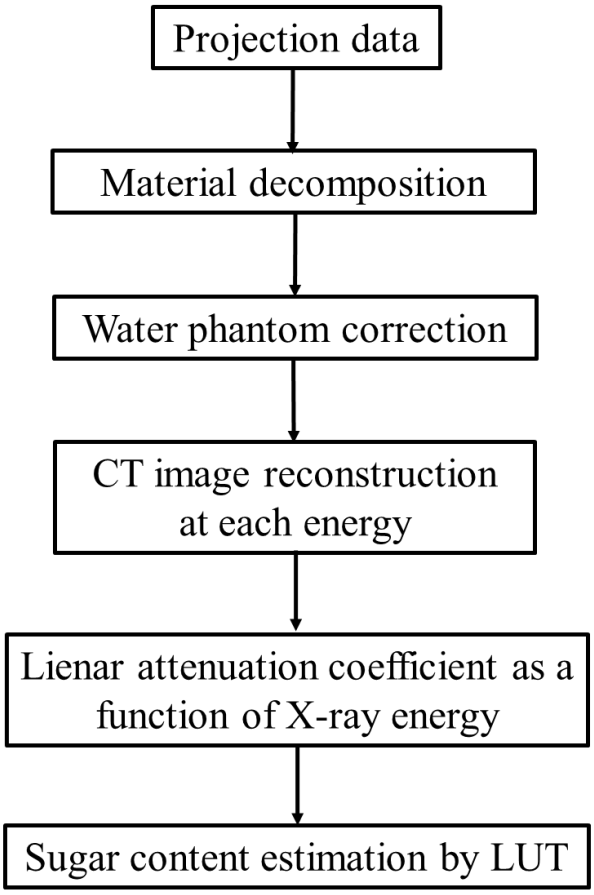

650

651

652 Figure 12

653

654

655

656

657

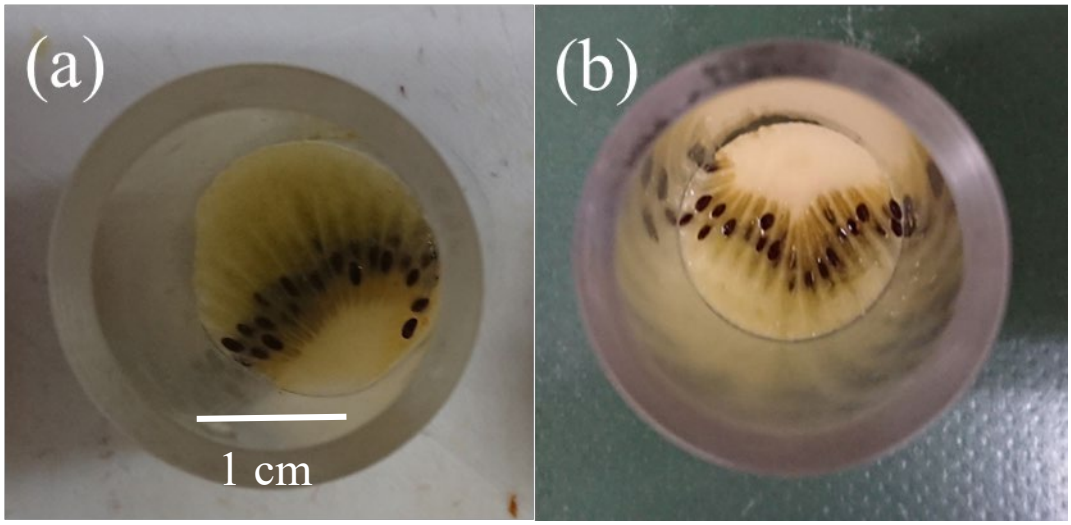

Figure 13

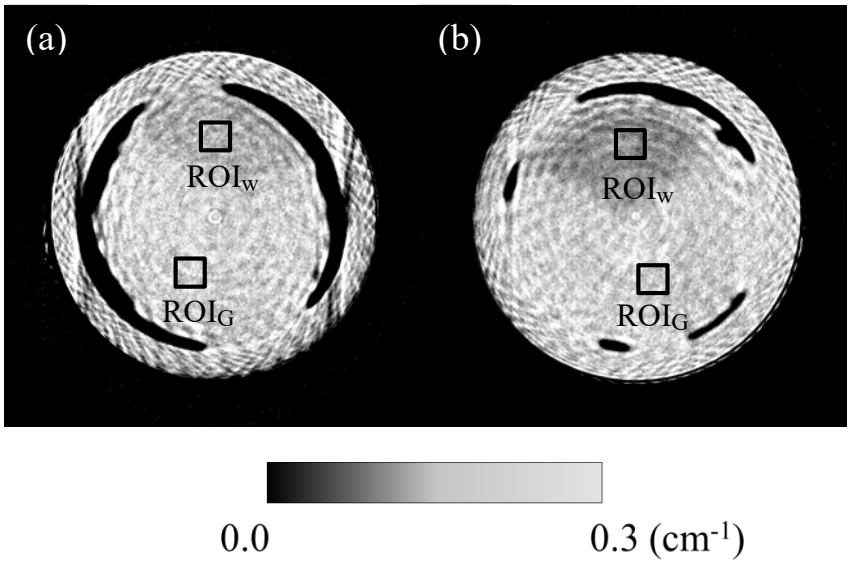

Figure 14

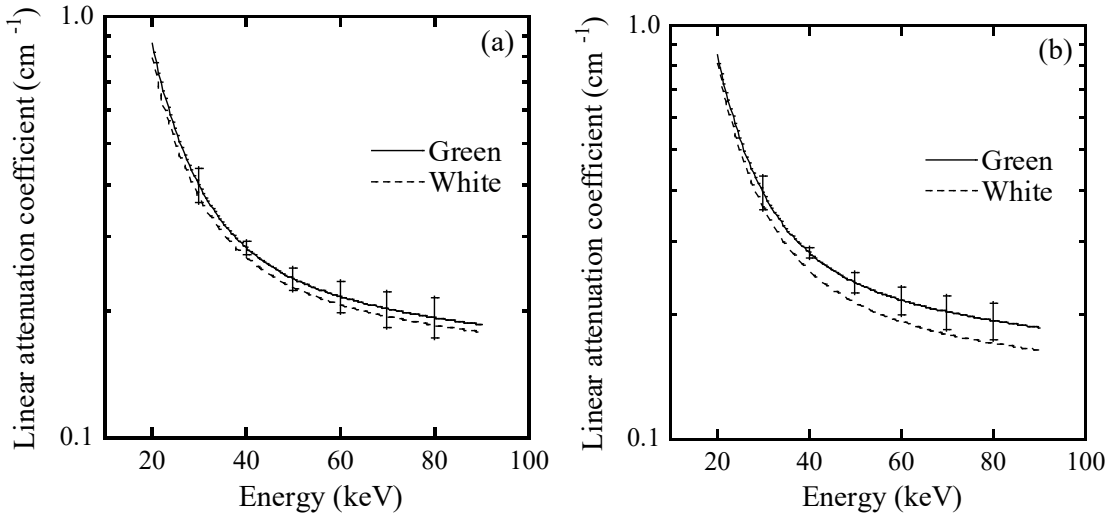

695

696

697

698 Figure 15

699

700

701

702

703

704

705

706

707

708

709

710

711